TiO$_2$ Nanotip Arrays: Anodic Fabrication and Field-Emission Properties
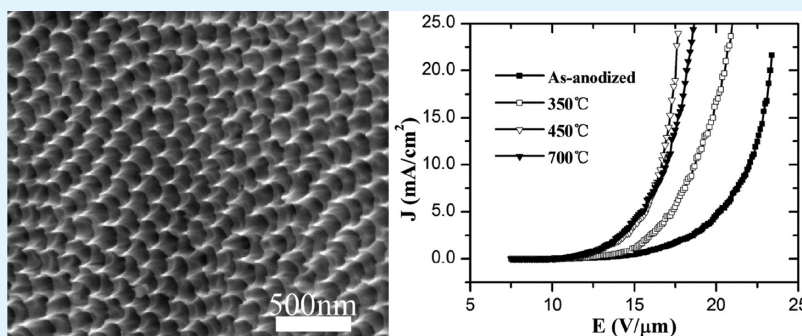
Jia Liang and Gengmin Zhang*

Key Laboratory for the Physics and Chemistry of Nanodevices and Department of Electronics, Peking University, Beijing 100871, China

S *Supporting Information*

ABSTRACT: In contrast to the main-stream strategy of growing convex nanostructures upward from the substrates and using them as cold electron sources, it is illustrated in this article that growing concave nanostructures downward into substrates also results in configurations suitable for field emission. Well-ordered TiO$_2$ nanotube arrays were developed on the titanium foils in two-step anodizations. Simultaneously, arrays of sharp nanotips, which resembled the Spindt emitter arrays in appearance, also manifested themselves on the outmost surface of the foils. These nanotips were actually the remainder of the titanium foil surfaces that survived dissolution during anodization. Annealing transformed the amorphous TiO$_2$ nanotips into anatase crystals and further to rutile. Despite the lack of an overall large aspect ratio, the sharpness of these nanotips guaranteed sufficiently strong electric fields for electron extraction. As a result, field emission was readily obtained from the TiO$_2$ nanotip arrays, either before or after annealing. Photoelectron spectroscopy of the samples demonstrated that the majority of the emitted electrons came from local states in the band gap. Annealing at an appropriate temperature increased these local states and improved the field-emission capability of the samples.

KEYWORDS: *TiO$_2$ nanotip, field emission, anodization, X-ray photoelectron spectrum, annealing*

1. INTRODUCTION

Field emission from nanomaterials has been under intense study for about 2 decades. In most studies, convex nanostructures, e.g., carbon nanotubes (CNTs) and metal oxide nanowires, are grown upward from substrates, and the local electric fields at their ends are often sufficiently strong for field emission to occur. One of the advantages of such a configuration is the large aspect ratio of the nanostructures, which generally leads to high field enhancement. Of course, the screening effect caused by their great length is sometimes a serious concern. Generally, the longer the nanostructures are, the larger the internanostructure separation must be to avoid the screening effect (see the Supporting Information, part I). Besides this main-stream strategy, "digging" of substrates, i.e., growing concave nanostructures downward into substrates, may also result in some configurations suitable for obtaining field emission. Anodization is one of the most effective approaches for growing concave nanostructures. In this context, titanium foils were anodized, and the products were subjected to field-emission study.

Anodic titanium dioxide (TiO$_2$) nanotubes are some of the most maturely developed metal oxide nanostructures fabricated by anodization. So far, as summarized by Su and Zhou,[1] the major applications of anodic TiO$_2$ nanotubes, either actual or potential, are in such areas as photocatalysis,[2] dye-sensitized solar cells (DSSCs),[3] gas sensing,[4] and biomedical engineering.[5] In contrast, reports on the field-emission properties of TiO$_2$ nanostructures, fabricated either by anodization or by other approaches, are relatively less abundant.[6−12]

As reported in this article, when titanium foils were subjected to appropriate anodizations, the generation of nanotube arrays also resulted in the formation of arrays of sharp protrusions on the outermost surfaces. Field emission was attainable from these sharp protrusions, around which the local electric fields were strong enough to extract electrons despite the lack of a large overall aspect ratio. The origin of the emitted electrons

was probed using a variety of analysis methods. Furthermore, properly controlled annealing was found to be an effective measure for improving the field-emission performance of the protrusion arrays.

2. EXPERIMENTAL METHODS

Detailed procedures for fabrication of the highly ordered TiO_2 nanotube arrays were given in a previous article published by this laboratory and are only briefly introduced here.[13] Ethylene glycol ($C_2H_6O_2$) containing 75 mM (0.25% in mass) NH_4F and 0.33 M (0.6% in volume) H_2O was used as the anodization electrolyte. In each reaction, a piece of titanium foil, 0.25 mm in thickness and 99.7% in purity, was used as the anodic metal after successive ultrasonic cleaning in acetone, ethanol, and deionized water. The titanium foil was attached to the positive electrode of a direct-current power source using an O-ring and copper plate. A piece of graphite was connected to the negative electrode and immersed in the electrolyte approximately 3 cm away from the titanium foil. All reactions were conducted at room temperature (25 °C).

For better ordering and alignment of the TiO_2 nanotube arrays, the titanium foil was anodized twice. The first anodization step was intended to provide a regular pattern on the titanium surface, which worked as a starting template for the second anodization. The titanium foil was first anodized under a 60 V voltage for 24 h. The TiO_2 nanotube array produced was removed ultrasonically, and the titanium foil, on whose surface a regular pattern remained, was again submitted to anodization at 60 V. The anodizing time was generally 12 h for the samples used in the field-emission study.

The samples were characterized using scanning electron microscopy (SEM), X-ray photoelectron spectroscopy (XPS), Raman spectroscopy (RS), and X-ray diffraction (XRD).

For the purpose of investigating the dependence of nanotube array morphology on the anodizing time in the second anodization, a small fraction of a sample was cut from the titanium foil and observed with SEM after the second anodization lasted different time intervals of 5, 10, and 30 min and 1 h, respectively.

In principle, the field-emission behavior of TiO_2 nanotube films remaining in situ on the titanium foil would not be much different from that of those adhered to other types of conducting substrates. However, the corrugation of the titanium foil surface could considerably disturb the measurement of field emission and mask the actual role of the nanotube arrays. Thus, after the conclusion of the second anodization, the TiO_2 nanotube arrays were allowed to detach spontaneously from the titanium substrate through rinsing in deionized water. The thereby-obtained free-standing TiO_2 nanotube arrays, 0.5−3 mm^2 in area, were then pasted onto silicon wafers, which were much flatter than the titanium foils, and used as the cathode in field-emission measurements (see the Supporting Information, part II).

The TiO_2 films fabricated by the present anodization method were all amorphous. To study the role of crystallization in the field emission, some samples were annealed in air at temperatures of 350, 450, 700, and 950 °C for 3 h with a ramp rate of 2 °C min^{-1}. The samples were left to cool naturally after annealing.

The resistances of the as-anodized and annealed TiO_2 nanotubes were estimated using two-point measurements. Metallic titanium layers were sputtered onto both the top and bottom sides of the nanotube arrays. In each measurement, the bottom side of the nanotube array was adhered to a metallic substrate and a probe was brought into contact with the top side of the nanotube array. A voltage ramp was applied between the probe and metallic substrate, and the current density was recorded. The resistances of the TiO_2 nanotube arrays were then determined from the current density−voltage curves.

The photoelectron spectra of the samples were also acquired using a photoelectron spectrometer in air (model AC-2, Riken Keiki). The energy of the incident UV photons was raised from 4.2 to 6.0 eV in 0.1 eV steps, and the number of photoelectrons was measured with an open-air counter.[14] The dependence of the photoelectron yield on the incident photon energy ($Y−E$ curves) provided information on the photoelectric thresholds and density of states (DOS) occupied by the electrons of the samples.

3. RESULTS AND DISCUSSION

3.1. Formation of the Nanotip Array. Similar to the previous work in this laboratory,[13] nanotube arrays with good orderliness and alignment were obtained by the controlled two-step anodization process. Figure 1 shows the SEM image of a
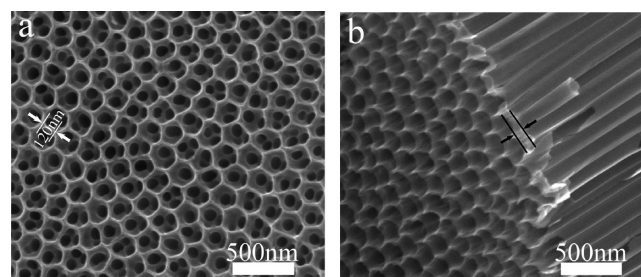

Figure 1. Nanotip array generated on the surface of a nanotube array fabricated by two-step anodization: (a) top view; (b) side view.

typical sample. It is notable that the nanotube array was covered by a nanoporous layer, highlighted by the arrows in Figure 1b. This amorphous layer may play multiple roles in a DSSC. On the one hand, the underneath nanotubes are more immune to etching when covered by such a nanoporous layer and thus have larger tube lengths;[15] on the other hand, the nanoporous layer could hinder the adsorption of dye molecules and absorption of incident light.[15,16] That is, the nanoporous layer plays a favorable role in the formation of the ordered TiO_2 nanotube arrays but an unfavorable role in their photovoltaic behavior. Consequently, the nanoporous layer is generally removed before a TiO_2 nanotubular film is used in a DSSC.[16−18] Interestingly, the nanoporous layer shown in Figure 1 was actually an assembly of upward-oriented nanotips, whose regular spatial arrangement and conic shape were immediately reminiscent of Spindt-type field-emitter arrays (FEAs).[19] The rapid development of Spindt-type FEAs in the last century opened up the research area "vacuum microelectronics". In contrast, in spite of the resemblance in morphology, the nanotip array shown in Figure 1 actually went well beyond the scope of "vacuum microelectronics". The nanotips were located at the vertices of hexagons, and the nearest-neighboring nanotips were separated by more than 100 nm, as indicated by the arrows in Figure 1a. This separation was obviously smaller than that between the cones of a Spindt-type FEA, the typical tip density of which is 6.4 × 10^7 cm^{-2} nowadays.[20] Moreover, the tips shown in Figure 1 were much sharper than those of Spindt-type emitters. Therefore, the study of these nanotips is considered to fall within the area of "vacuum nanoelectronics". Compared with the one-dimensional materials often used in vacuum nanoelectronics, e.g., CNTs and different kinds of nanowires, these TiO_2 nanotips appeared to have much lower overall aspect ratios because they were much shorter. However, the long length of one-dimensional materials often leads to a "screening effect" and/or entanglement, which seriously lowers the local electric field around the emitter ends if the individual emitters are not sufficiently separated from each other.[21] Also, the end shape is sometimes more important than the overall aspect ratio in determining the local field strength.[22] It is then quite reasonable to expect good field-emission performances from

6054

dx.doi.org/10.1021/am301690f | ACS Appl. Mater. Interfaces 2012, 4, 6053−6061

the present TiO_2 nanotips with sharp ends, high density, and suitable separation.

To gain an understanding of the formation mechanism of this kind of nanotip array, a titanium foil surface that had been subjected to the first-step anodization was observed after different second-step anodization times. The results are given in Figure 2. As shown in Figure 2a, after removal of the TiO_2
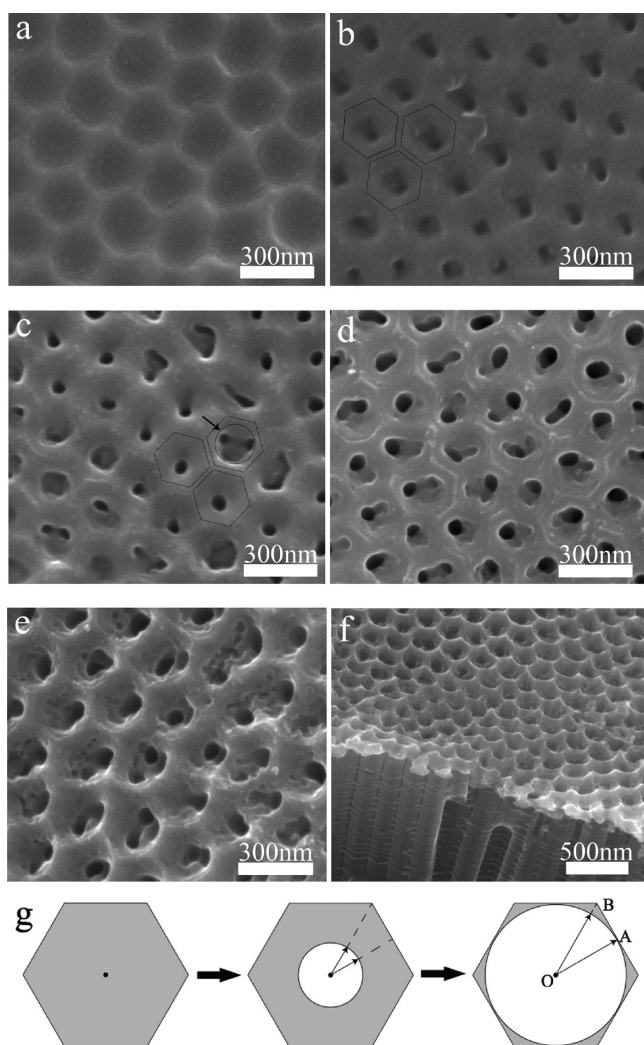

Figure 2. SEM images of the titanium foil surface after different anodization times at 60 V for the second-step anodization: (a) titanium foil surface after removal of the TiO_2 nanotube film generated by the first-step anodization; (b) titanium foil surface after the second-step anodization lasted 5 min, (c) 10 min, (d) 30 min, and (e) 1 h; (f) side view of part e; (g) formation mechanism of a nanotip array ("A" represents the middle point of a hexagon edge, and "B" represents a hexagon vertex).

nanotube arrays generated in the first-step anodization, a regular hexagon-shaped pattern was left on the titanium foil surface. Figure 2b shows that the titanium surface underwent a dramatic change even when the second-step anodization had lasted only 5 min: small pits emerged at the centers of the hexagons. Moreover, the edges of the hexagons were also partially flattened, and the boundaries between the hexagons became unclear. As shown in Figure 2c, the pits further deepened and expanded when the anodization time was extended to 10 min. The deepening of the pits finally resulted

in formation of the nanotube array. The etched region in each hexagon on the titanium surface can be roughly defined as a circle, as indicated by the arrow in Figure 2c. The circular shape of the etched region suggested an approximate equality of the expansion speed of the etched region, with respect to the center of the hexagon, along all directions across the horizontal surface.

As shown in Figure 2d–f, the incessant etching continued when the anodization time was further prolonged to 30 min and 1 h. In terms of the degree to which a location was etched, the surface could be broadly classified into three regions, which were the inner parts, the edges, and the vertices of the hexagons. The inner parts of the hexagons were the most severely etched regions, while the etching of the edge regions was much less severe and that of the vertex regions was the slightest. The eventual formation of the nanotips at the vertices of the hexagons was actually a consequence of this spatial disparity in the etching.

As summarized by Su et al.[1] and Roy et al.,[23] formation of the TiO_2 nanotube array resulted from competition between oxidation of titanium and dissolution of TiO_2.

The small amount of water in the electrolyte dissociated at the anode to produce O^{2-} anions by field-assisted deprotonation:[1]

$$H_2O \rightarrow OH^- + H^+ \qquad (1)$$

$$OH^- \rightarrow O^{2-} + H^+ \qquad (2)$$

Metallic titanium at the anode gave up electrons to produce Ti^{4+} cations, some of which encountered the O^{2-} anions and generated TiO_2:

$$Ti + 2O^{2-} \rightarrow TiO_2 + 4e^- \qquad (3)$$

The high electric field across the oxide layer played a key role in the expansion of the oxide layer into the interior of the titanium foil. First, the high field drove the O^{2-} anions to migrate from the electrolyte/oxide interface to the oxide/titanium interface through the oxide layer, so that the metallic titanium was continuously oxidized as described in eq 3. Second, Ti^{4+} cations that did not react with the O^{2-} anions were ejected directly into the electrolyte by the high field, giving more room for the growing oxide layer.[24]

The high field was available only if the oxide layer was kept sufficiently thin. That is, the oxide layer was simultaneously etched at the oxide/electrolyte interface when it was growing at the metal/oxide interface. The etching resulted from both chemical dissolution and high-field-assisted dissolution. In the direct chemical attack, the fluoride in the electrolyte converted TiO_2 into water-soluble $[TiF_6]^{2-}$ cations:[23,25]

$$TiO_2 + 6F^- + 4H^+ \rightarrow [TiF_6]^{2-} + 2H_2O \qquad (4)$$
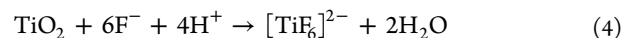
Also, complexation occurred between the F^- anions in the electrolyte and the Ti^{4+} cations ejected into the electrolyte through the oxide layer:[23]

$$Ti^{4+} + 6F^- \rightarrow [TiF_6]^{2-} \qquad (5)$$

As will be expounded in the following discussion, this etching of the TiO_2 layer played a key role in formation of the nanotip arrays.

In the equifield strength model proposed by Su et al.,[26] the dissolution, which transformed the otherwise nonporous oxide layer first into a hemispherical pore bottom and then into a

nanotube array, was initiated by defects in the oxide layer having random locations. Though the tendency of the field to maintain equality across the oxide layer resulted in some degree of self-ordering, the orderliness and uniformity of the nanotube array was generally unsatisfactory. In the present two-step anodization, in contrast, the pattern left on the titanium surface after detachment of the nanotube array generated in the first-step anodization constituted a relatively ordered template for the initial dissolution to occur. Consequently, the nanotube array generated in the second-step anodization was well-ordered.

On the basis of the results presented in Figure 2b–f, the formation mechanism of the obtained nanotip arrays is proposed in Figure 2g. As observed from above, the anodized TiO$_2$ array had a hexagonal unit cell. When they continuously grew deeper into the titanium foils, the nanotubes simultaneously became thicker. That is, besides the major direction toward the interior of the titanium foil, the etching of the TiO$_2$ layer also had components to the surroundings of the hexagon center, denoted by "O", along the titanium surface.

In a rough approximation, the speed of the expansion of the etched region from the center "O" is considered to have been isotropic across the foil surface. This approximation is supported by the results shown in Figure 2b–e. Obviously, the distance between each point on the boundary of the hexagon and "O" was not equal. The points nearest to the center on the boundary were the middle points of the edges, represented by "A" in Figure 2g, while the farthest points were the vertices, represented by "B". When the etched region expanded to reach point A, as indicated by the circle, point B still remained relatively uninfluenced. Because of this disparity in the spatial distance from each center, the vertex regions in the array of hexagons survived the etching and became the highest parts on the surface, resulting in the eventual formation of the nanotip array.

3.2. Annealing Treatment. Annealing is an often-used postanodization treatment for TiO$_2$. For example, when employed in a DSSC, TiO$_2$ must first be crystallized by annealing to lower the number of traps and recombination centers.[18,27] In this work, samples were annealed in an effort to improve their field-emission performance. To investigate possible annealing-caused changes in the morphology, chemical composition, and crystallinity of the samples, SEM, XPS, RS, and XRD analyses were correspondingly carried out.

As shown in Figure 3, the orderliness of the nanotip array survived annealing at up to 700 °C. After annealing at 950 °C, the sample peeled off from the substrate and became unsuitable for field emission.

XPS results for an as-anodized sample and samples annealed at different temperatures are collectively shown in Figure 4. The spectra were dominated by the photoelectron lines of titanium and oxygen. The C 1s line, generally believed to have arisen from adventitious carbon caused by exposure to the atmosphere, was also found in the spectra of all samples and used as the standard for calibration during data processing. Moreover, two fluorine lines found in the spectrum of the as-anodized sample disappeared after annealing, suggesting that they originated from a residual F-containing electrolyte on the samples. With the energy of the C 1s line set at 284.6 eV, the energies of the Ti 2p$_{1/2}$ and 2p$_{3/2}$ lines were determined after calibration and are listed in Table 1a. Energies of the 2p$_{1/2}$ and 2p$_{3/2}$ lines of oxidized titanium obtained by some previous researchers are given in Table 1b.
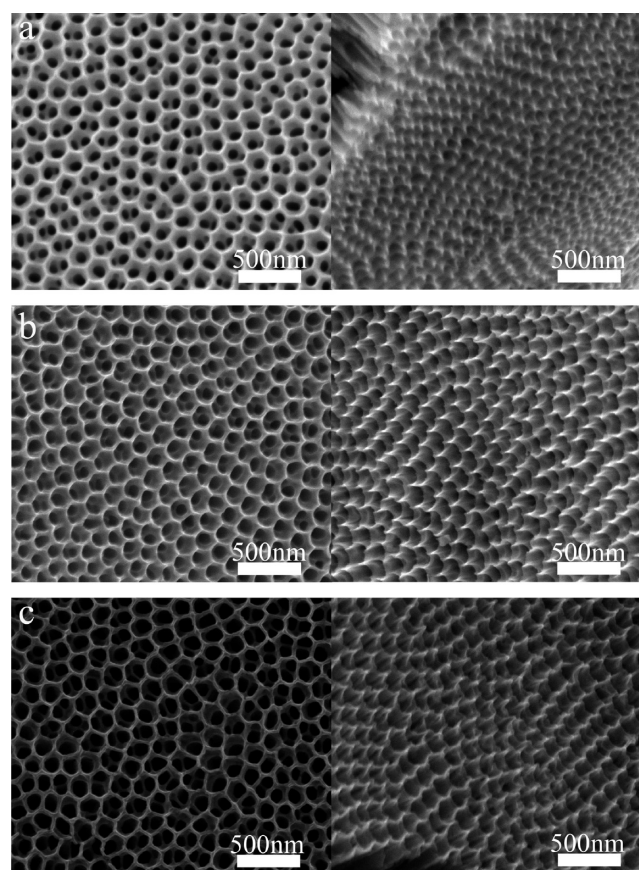

Figure 3. SEM images of the samples after annealing at (a) 350, (b) 450, and (c) 700 °C, respectively.

A number of oxides of titanium with different Ti–O stoichiometric compositions are possible. Fortunately, as shown in Table 1b, the chemical shifts of the titanium lines increase both considerably and monotonously with the percentage of oxygen in the oxides, making it possible to determine the particular oxides obtained in this work. The chemical shifts, shown in Table 1a, of the Ti 2p$_{1/2}$ and Ti 2p$_{3/2}$ lines were as large as 4.3–4.8 and 4.4–5.0 eV, respectively, in this work, quite similar to those of standard titanium dioxide and much larger than those of other oxides of titanium. Therefore, the XPS results indicated that the chemical composition of the nanotubes produced in this work was titanium dioxide and that annealing did not lead to an obvious change in composition.

Besides the chemical composition, oxides of titanium often need to be further characterized by their crystal structures. A TiO$_2$ sample can be amorphous, anatase, rutile, or brookite. To determine whether and how the annealing treatment crystallized the TiO$_2$ nanotip arrays, further analysis was necessary. Both the anatase TiO$_2$ and the rutile TiO$_2$ are networks of TiO$_6$ octahedra and belong to the tetragonal crystal system whose point group is D_{4h} ($4/m\ 2/m\ 2/m$).[32] However, the arrangement and coordination of the octahedra are different in them. The lattice constants of the conventional unit cell of the anatase TiO$_2$ are a = 0.3785 nm and c = 0.9514 nm. Those of the rutile TiO$_2$ are a = 0.4594 nm and c = 0.2959 nm.[33] The space group of the anatase TiO$_2$ is D_{4h}^{19} ($I4_1/amd$) and that of the rutile TiO$_2$ is D_{4h}^{14} ($P4_2/mnm$).[34] Therefore, besides the XRD pattern, the anatase TiO$_2$ and rutile TiO$_2$ also have well-distinct Raman fingerprints.[34] As pointed out by Ohsaka et al.,
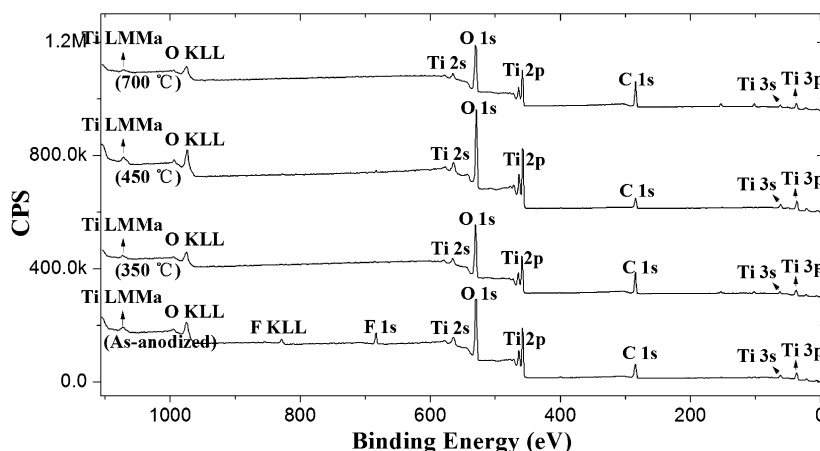
Figure 4. Results of XPS analysis of the nanotubes before and after annealing.

Table 1. Ti 2p Photoelectron Lines Obtained in This Work and Those from Previous Literature[a]

	(a) This Work	
	$2p_{1/2}$ (eV)	$2p_{3/2}$ (eV)
as-anodized	464.6 (4.6)	458.7 (4.7)
350 °C	464.75 (4.8)	458.95 (5.0)
450 °C	464.3 (4.3)	458.4 (4.4)
700 °C	464.75 (4.8)	458.95 (5.0)
	(b) In Previous Literature	
	$2p_{1/2}$ (eV)	$2p_{3/2}$ (eV)
Ti[28]*	460.0*	454.0*
TiO[29]	460.2 (0.2)	454.6 (0.6)
Ti$_2$O$_3$[29]	462.0 (2.0)	456.8 (2.8)
TiO$_2$	464.6 (4.6),[29] 464.5 (4.5),[30] 464.3 (4.3)[31]	458.9 (4.9),[29] 458.6 (4.6),[30] 458.6 (4.6)[31]

[a]Values in brackets are chemical shifts with respect to metallic titanium, as highlighted by asterisks in part b.

among all optical modes of the anatase TiO$_2$, one A$_{1g}$ mode, two B$_{1g}$ modes, and three E$_g$ modes are Raman-active.[35] In contrast, Porto et al. assigned four Raman-active modes to A$_{1g}$, B$_{1g}$, B$_{2g}$, and E$_g$ symmetries.[32] These differences in the lattice constants and symmetry make RS a powerful tool for identifying TiO$_2$ crystal structures. The RS results of the as-anodized and annealed samples are given in Figure 5 and Table 2. XRD patterns are shown in Figure 6.

The RS and XRD patterns of the as-anodized sample did not exhibit any vibration or diffraction peaks, respectively, confirming the amorphousness of the direct products of the titanium anodization.

In Figure 5, the RS of the samples annealed at 350, 450, and 700 °C all exhibited peaks at 143, 394, 515, and 638 cm^{-1}, with the 143 cm^{-1} peak being prominently higher than the others. A comparison of the positions and relative intensities of the above peaks with the results obtained by previous researchers shows that these Raman lines were caused by vibrations in the anatase TiO$_2$ crystal.[36] Especially, the dominant 143 cm^{-1} line was attributed to the low-frequency O−Ti−O bending vibration.[37] The B$_{1g}$(1) and E$_g$(2) modes of the anatase TiO$_2$ given in Table 2 were also the O−Ti−O bending-type vibrations. The E$_g$(3), A$_{1g}$, and B$_{1g}$(2) modes were of the Ti−O stretching-type vibrations.[35] Correspondingly, as shown in Figure 6, the XRD patterns of the samples annealed at 350, 450, and 700 °C all contained peaks due to crystal planes with interplanar spacings
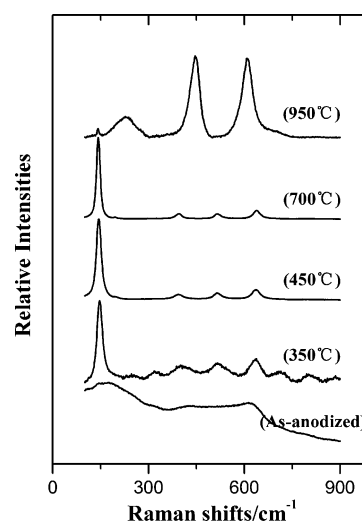

Figure 5. RS of the as-anodized and annealed samples.

Table 2. Raman-Active Vibrations of TiO$_2$[a]

Anatase TiO$_2$ (Tetragonal, Six Raman-Active Modes)						
mode	A$_{1g}$	B$_{1g}$(1)	B$_{1g}$(2)	E$_g$(1)	E$_g$(2)	E$_g$(3)
peak positions (cm^{-1}) ref 34	519	399	519	144	197	639
this work	515	394	515	143	not found	638
Rutile TiO$_2$ (Tetragonal, Four Raman-Active Modes)						
mode	A$_{1g}$		B$_{1g}$	B$_{2g}$		E$_g$
peak positions (cm^{-1}) ref 34	612		143	826		447
this work	609		142	not found		446

[a]In this work, shifts of the Raman lines to the low-frequency end were largely due to a low accuracy in calibration.

of 3.51, 2.38, 1.89, 1.70, 1.67, and 1.48 Å. All of these crystal planes can be found in the anatase TiO$_2$ crystal.[38] It was therefore concluded that the annealing transformed the amorphous TiO$_2$ nanotube arrays into anatase crystals. As summarized by Hanaor and Sorrell, the phase transition from anatase to rutile in air is widely believed to begin at ∼600 °C. Nevertheless, the transition temperature could vary from 400 up to 1200 °C, depending on experimental conditions and measurement methods.[33] For example, according to Fang et al's observation, although the TiO$_2$ nanotubes on the titanium
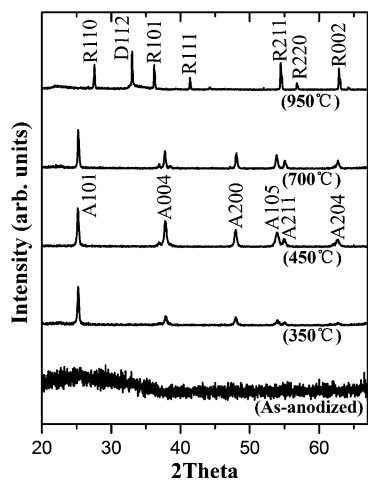
Figure 6. XRD patterns of the as-anodized and annealed samples ("A" represents anatase; "R" represents rutile; "D" represents dititanium trioxide).

substrate transformed from anatase to rutile at 600 °C, a free-standing TiO_2 membrane retained the anatase phase until the annealing temperature rose to 800 °C.[39] Therefore, the result in this work that the TiO_2 nanotip array remained mainly in the anatase phase up to 700 °C appeared to be in agreement with some previous reports.

The RS of the sample changed dramatically after annealing at 950 °C. The resulting peaks at 142, 446, and 609 cm^{-1} were all ascribable to the vibrations in the rutile TiO_2.[36] In the rutile TiO_2, the B_1 mode is an out-of-plane vibration mode, just as in the anatase TiO_2. The A_1 and B_2 modes predominantly resulted from Ti−O stretching and in-plane deformation, respectively.[40] Noticeably, the 142 cm^{-1} vibration was considerably lower than the 143 cm^{-1} vibration observed for the anatase TiO_2, in agreement with some previous researchers' results.[37] Moreover, the broad band at around 227 cm^{-1} was attributable to Ti_2O_3.[41] Most of the peaks in the XRD pattern of the 950 °C annealed sample were generated by crystal planes with interplanar spacings of 3.25, 2.49, 1.69, 1.62, and 1.36 Å, coinciding with the crystalline structure of the rutile TiO_2.[42] The strongest peak was generated by the 2.71-Å-spaced crystal planes, which corresponded to the (112) plane of the rhombohedral Ti_2O_3 crystal.[43] Therefore, both the RS and XRD results suggested a

transformation from anatase to rutile TiO_2 and rhombohedral Ti_2O_3 during annealing at 950 °C.

The dependence of the electrical properties of the TiO_2 nanotube arrays on the annealing temperature is given in Figure 7. Noticeably, the resistance of the 450 °C annealed sample was considerably lower than that of the other samples. This result, which was in rough agreement with those reported by previous researchers,[44] is tentatively attributed to the phase transition of TiO_2. It has been well-established that the rutile TiO_2 is far more resistive than the anatase TiO_2.[23] Annealing at temperatures of up to 450 °C transformed the amorphous TiO_2 into anatase, resulting in a decrease in the resistance. The failure of the RS and XRD analyses to indicate a detectable increase of the percentage of anatase in the sample when the annealing temperature was raised from 350 to 450 °C was possibly due to limited sensitivities. Similarly, although the transition from anatase to rutile TiO_2 was not obviously detected in the RS and XRD analyses until the annealing temperature rose to 950 °C, the observed increase of the resistivity caused by annealing at 700 °C was believed to have resulted from a partial transition from anatase to rutile TiO_2 (Supporting Information, part III). Quite naturally, the resistivity of the 950 °C annealed sample, in which the rutile TiO_2 was already the major phase, was obviously higher than those of the samples annealed at lower temperatures.

In terms of the electron energy distribution, the field-emission current density is not solely determined by the most energetic occupied level, the difference between which and the vacuum level is crudely referred to as the "work function" under certain circumstances, but also by the electron density in its vicinity. As is common knowledge, the conductivity is determined by both the density and mobility of the carriers. In this regard, the resistivity measurements provided important clues on the field emission-related electron energy distribution. More decisive knowledge was subsequently obtained from photoelectron spectrometry.

Figure 8a shows the dependence of the photoelectron yield of the samples on the incident photon energy. The most important function of a photoelectron spectrum seems to be determination of the threshold energy for photoelectric emission.[14,45] For a metal, the square root of the photoelectron yield increases linearly with the energy of the incident photon above the work function.[46] For a semiconductor, a linear
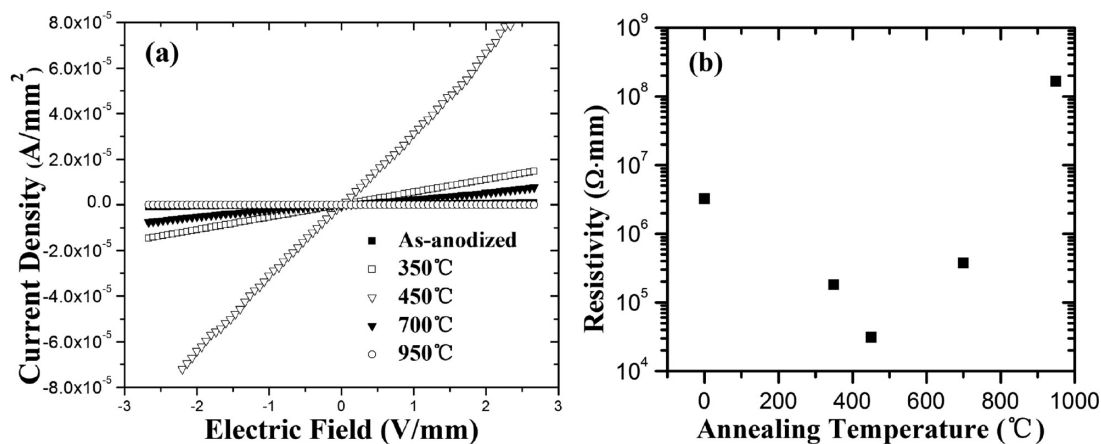

Figure 7. Dependence of the electrical properties of the TiO_2 nanotube arrays on the annealing temperature: (a) current density; (b) resitivity (annealing temperature "0 °C" means no annealing).
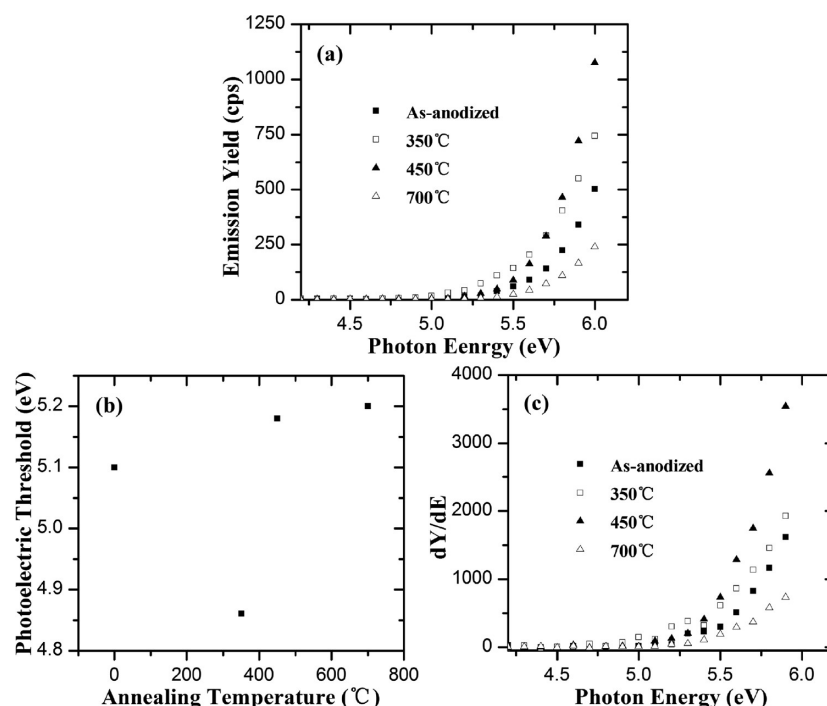
Figure 8. Photoelectron spectra of the as-anodized and annealed samples: (a) photoelectric emission yield versus photon energy; (b) work functions of the samples before and after annealing (annealing temperature "0 °C" means no annealing); (c) derivative of the yield versus photon energy.
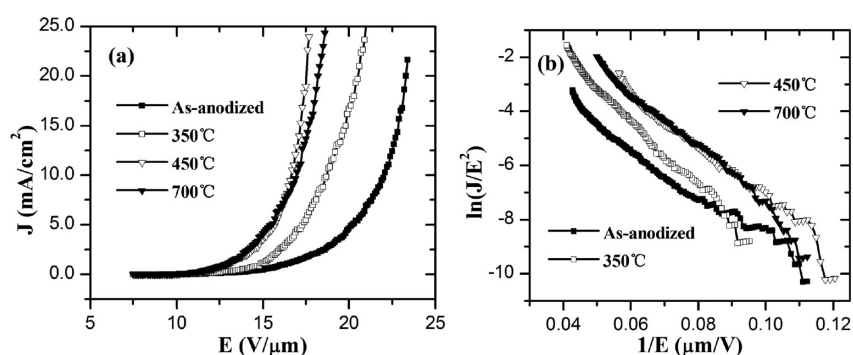

Figure 9. Field-emission properties of the as-anodized and annealed TiO$_2$ nanotip arrays: (a) J–E curves; (b) FN plots.

relationship emerges between the cubic root of the yield and the photon energy above the threshold of photoelectric emission.[47] As shown in Figure 8b, by following this empirical practice, the thresholds of the photoelectric emission of the samples were all determined to be around 5 eV within a range of 0.3 eV.

It is generally believed that the band gap of TiO$_2$ is larger than 3 eV.[23] The electron affinity of TiO$_2$ is larger than 4 eV, and the valence band edge is about 7.5 eV below the vacuum level.[48] Therefore, the major states that contributed to the photoelectric emission shown in Figure 8a must have come from the energy levels within the band gap, which were presumably caused by the presence of such defects as oxygen vacancies and Ti^{3+} states.[23]

Besides providing the photoelectric threshold, a photo-electron spectrum can also be used to estimate the DOS occupied by electrons of a sample by differentiating the yield by the photon energy.[49] In this work, the differential of the yield was approximated by the difference between the yields at two neighboring photon energies. The quotient of this difference to the step of the photon energy increase, 0.1 eV, was used to

estimate the derivative of the yield with respect to the photon energy. For example, for the as-anodized sample, the yields at photon energies of 5.3 and 5.4 eV were 18.2 and 38.5, respectively. The derivative at 5.3 eV was then approximated by

$$\frac{38.5 - 18.2}{0.1} = 203$$

The yield derivative (dY/dE) versus photon energy curves are shown in Figure 8c. Although the highest occupied energy levels of all of the samples did not differ significantly, which can be seen from Figure 8b, the disparity in the DOS was quite considerable.

When the amorphous TiO$_2$ was transformed into anatase by annealing at 350 and 450 °C, the DOS increased. Annealing at higher temperature, which presumably introduced a greater percentage of rutile to the sample, lowered the DOS. This variation of the DOS was in agreement with both the previous researchers' results[23] and the preceding result of the resistance measurements.

3.3. Field-Emission Properties. The field-emission properties of the as-anodized and annealed TiO$_2$ nanotip

Table 3. Turn-On and Threshold Fields of the As-Anodized and Annealed TiO$_2$ Nanotip Arrays

	annealing temperature (sample area)			
	as-anodized (3.7 mm^2)	350 °C (0.6 mm^2)	450 °C (3.8 mm^2)	700 °C (1.5 mm^2)
turn-on field(V/μm)	9.4–9.5	10.5–10.8	8.6–8.7	9.0–9.4
first threshold field(V/μm)	16.3–16.6	14.6–14.9	12.8	12.9–13.1
second threshold field(V/μm)	21.2–22.1	18.6–18.8	16.6–16.7	17.0

arrays are illustrated in Figure 9. Figure 9a shows the dependence of the field-emission current density on the average electric field (J–E curves). Figure 9b shows the Fowler–Nordheim (FN) plots, whose approximate linearity confirmed that the electron emission from the samples was a result of electron tunneling. The turn-on and threshold fields are listed in Table 3. The turn-on field is defined as the average field between the cathode and anode to extract 10 μA/cm^2 current density.[50] The threshold field is defined as the average field to extract a current density sufficient for related devices to operate. The value of this current density is considered to be either 1 or 10 mA/cm^2, depending on the practical applications. In this article, the threshold field to extract a current density of 1 mA/cm^2 is termed the "first threshold field" and that to extract 10 mA/cm^2 the "second threshold field".[50,51] (Supporting Information, part IV).

The results given in Figure 9 and Table 3 confirmed that the TiO$_2$ nanotips fabricated by the anodizing of titanium foils could indeed deliver electrons under moderately high field because of the sharpness of their ends. It was also demonstrated that annealing at an appropriate temperature effectively improved the field-emission capability of the sample and that the optimal annealing temperature appeared to be around 450 °C.

Even the largest resistance observed was lower than 0.1 MΩ (Supporting Information, part V). Thus, the largest voltage drop across the emitters during field emission, in which the largest obtained current was around 0.8 mA, was less than 0.1 kV. That is, the voltage drops across the samples were not a serious concern and the actual voltages applied to the emitter surfaces were not significantly lower than the output voltages of the power source. Therefore, the disparity in the performance of the field emission was not directly caused by the resistances.

Furthermore, the thresholds for the photoelectric emission given in Figure 8b were not in good accordance with the field-emission properties of the samples. For instance, the sample with the best field-emission performance, which had been annealed at 450 °C, did not show the lowest-energy threshold for photoelectric emission. In FN theory, which is the most frequently used theory for interpreting field-emission phenomena, the field-emission current density is determined by two factors, namely, the external field and the work function of the emitter. That is, the intrinsic properties of an emitter are solely represented by the work function. Therefore, the results presented in Table 3 and Figure 8b actually contradicted the traditional FN theory (Supporting Information, part VI).

Instead, the yield derivative–photon energy curves shown in Figure 8c were found to be suitable in interpreting the disparity in the field-emission performance of the samples. According to the results presented in Figure 8, the photoelectric emission was not available until the photon energy was as high as around 5 eV, indicating that the density of the electrons in the conduction band was low. Although they caused the TiO$_2$ nanotube arrays to behave differently from an insulator, these electrons in the conduction band were still too sparse to constitute the major part of the photocurrent. (For this reason, the electrons in the conduction band were disregarded for the discussion of the "highest occupied energy level" below.) It is, hence, logical to speculate that the electrons emitted from the conduction band only accounted for a negligibly small fraction of the field-emission current. Meanwhile, the electrons in the valence band faced a barrier both too high and too thick to penetrate. Consequently, it is believed that the electrons of the field-emission current mainly originated from the localized energy levels within the band gap. The estimated DOS of the 450 °C annealed sample was obviously higher than those of the other samples, echoing the fact that the turn-on and threshold fields of this sample were the lowest among all of the samples. The agreement between the field-emission capability and the estimated DOS was found to be quite reasonable. The larger the DOS, the more electrons were able to meet the barrier of relatively smaller height and thickness and thus contribute to the field emission. Both the position of the highest occupied energy level and the DOS just below it were crucial factors that could determine the field-emission capability of a sample. Figures 7 and 8 demonstrated that the annealing process in this work brought about very limited change in the highest occupied energy level but led to considerable variation in the DOS. When the samples were crystallized into the anatase TiO$_2$ from amorphous TiO$_2$ because of annealing at the appropriate temperature, high-density donors were generated.[52] Annealing at even higher temperature increased the percentage of less conductive rutile TiO$_2$, resulting in a lower DOS in the band gap.

4. CONCLUSION

When the anodization of titanium foils was properly controlled, ordered TiO$_2$ nanotip arrays were obtained as byproducts of the formation of the nanotube arrays. Field emission was readily available from these nanotube arrays, suggesting that the strategy of growing concave nanostructures downward into metal substrates is also effective in fabricating nanometer-scale field emitters. Annealing crystallized the nanotip arrays without causing obvious changes in their morphology and chemical composition. The transition from amorphous to anatase crystalline TiO$_2$ under annealing at the appropriate temperatures increased the local DOS occupied by electrons in the band gap and improved the field-emission capability of the samples.

■ ASSOCIATED CONTENT

⑤ Supporting Information

Screening effect, transfer of TiO$_2$ nanotube films from Ti foils onto Si substrates, detecting the phase composition of TiO$_2$, ambiguity in the "electric field" and "current density", resistances of the samples in the field-emission measurement, and validity of FN theory in this work. This material is available free of charge via the Internet at http://pubs.acs.org.

6060

dx.doi.org/10.1021/am301690f | ACS Appl. Mater. Interfaces 2012, 4, 6053–6061

■ AUTHOR INFORMATION

Corresponding Author
*E-mail: zgmin@pku.edu.cn.

Notes
The authors declare no competing financial interest.

■ REFERENCES

(1) Su, Z. X.; Zhou, W. Z. *J. Mater. Chem.* **2011**, *21*, 8955−8970.

(2) Atyaoui, A.; Bousselmi, L.; Cachet, H.; Pu, P.; Sutter, E. M. M. *J. Photochem. Photobiol. A* **2011**, *224*, 71−79.

(3) Ji, Y. J.; Lin, K. C.; Zheng, H. G.; Liu, C. C.; Dudik, L.; Zhu, J. J.; Burda, C. *ACS Appl. Mater. Interfaces* **2010**, *2*, 3075−3082.

(4) Paulose, M.; Varghese, O. K.; Mor, G. K.; Grimes, C. A.; Ong, K. G. *Nanotechnology* **2006**, *17*, 398−402.

(5) Ma, M. H.; Kazemzadeh-Narbat, M.; Hui, Y.; Lu, S. S.; Ding, C. F.; Chen, D. D. Y.; Hancock, R. E. W.; Wang, R. Z. *J. Biomed. Mater. Res., Part. A* **2012**, *100A*, 278−285.

(6) Yin, H.; Luo, M.; Yu, K.; Gao, Y. F.; Huang, R.; Zhang, Z. L.; Zeng, M.; Cao, C. X.; Zhu, Z. Q. *ACS Appl. Mater. Interfaces* **2011**, *3*, 2057−2062.

(7) Wang, C. C.; Wang, K. W.; Perng, T. P. *Appl. Phys. Lett.* **2010**, *96*, 143102−1−3.

(8) Xu, X. J.; Tang, C. C.; Zeng, H. B.; Zhai, T. Y.; Zhang, S. Q.; Zhao, H. J.; Bando, Y.; Golberg, D. *ACS Appl. Mater. Interfaces* **2011**, *3*, 1352−1358.

(9) Miyauchi, M.; Tokudome, H.; Toda, Y.; Kamiya, T.; Hosono, H. *Appl. Phys. Lett.* **2006**, *89*, 043114-1−043114-3.

(10) Alivov, Y.; Klopfer, M.; Molloi, S. *Appl. Phys. Lett.* **2010**, *96*, 243502-1−243502-3.

(11) Yang, Y.; Wang, X. H.; Sun, C. K.; Li, L. T. *J. Am. Ceram. Soc.* **2008**, *91*, 4109−4111.

(12) Ding, J. J.; Yan, X. B.; Li, J.; Shen, B. S.; Yang, J.; Chen, J. T.; Xue, Q. J. *ACS Appl. Mater. Interfaces* **2011**, *3*, 4299−4305.

(13) Li, S. Q.; Zhang, G. M.; Guo, D. Z.; Yu, L. G.; Zhang, W. *J. Phys. Chem. C* **2009**, *113*, 12759−12765.

(14) Kirihata, H.; Uda, M. *Rev. Sci. Instrum.* **1981**, *52*, 68−70.

(15) Yasuda, K.; Macak, J. M.; Berger, S.; Ghicov, A.; Schmuki, P. *J. Electrochem. Soc.* **2007**, *154*, C472−C478.

(16) Kim, D.; Ghicov, A.; Schmuki, P. *Electrochem. Commun.* **2008**, *10*, 1835−1838.

(17) Wang, D. A.; Liu, Y.; Yu, B.; Zhou, F.; Liu, W. M. *Chem. Mater.* **2009**, *21*, 1198−1206.

(18) Li, S. Q.; Liu, Y. M.; Zhang, G. M.; Zhao, X. Z.; Yin, J. B. *Thin Solid Films* **2011**, *520*, 689−693.

(19) Spindt, C. A.; Brodie, I.; Humphrey, L.; Westerberg, E. R. *J. Appl. Phys.* **1976**, *47*, 5248−5263.

(20) Xu, N. S.; Huq, S. E. *Mater. Sci. Eng. Res.* **2005**, *48*, 47−189.

(21) Nilsson, L.; Groening, O.; Emmenegger, C.; Kuettel, O.; Schaller, E.; Schlapbach, L.; Kind, H.; Bonard, J. M.; Kern, K. *Appl. Phys. Lett.* **2000**, *76*, 2071−2073.

(22) Xiao, J.; Zhang, X. X.; Zhang, G. M. *Nanotechnology* **2008**, *19*, 295706-1−295706-6.

(23) Roy, P.; Berger, S.; Schmuki, P. *Angew. Chem., Int. Ed.* **2011**, *50*, 2904−2939.

(24) Su, Z. X.; Zhou, W. Z. *J. Mater. Chem.* **2009**, *19*, 2301−2309.

(25) Mor, G. K.; Varghese, O. K.; Paulose, M.; Shankar, K.; Grimes, C. A. *Sol. Energy Mater. Sol. Cells* **2006**, *90*, 2011−2075.

(26) Su, Z. X.; Hahner, G.; Zhou, W. Z. *J. Mater. Chem.* **2008**, *18*, 5787−5795.

(27) Ghicov, A.; Schmuki, P. *Chem. Commun.* **2009**, 2791−2808.

(28) Ermolieff, A.; Bernard, P.; Marthon, S.; Wittmer, P. *Surf. Interface Anal.* **1988**, *11*, 563−568.

(29) Gonbeau, D.; Guimon, C.; Pfisterguillouzo, G.; Levasseur, A.; Meunier, G.; Dormoy, R. *Surf. Sci.* **1991**, *254*, 81−89.

(30) Bond, G. C.; Flamerz, S. *Appl. Catal.* **1989**, *46*, 89−102.

(31) Fierro, J. L. G.; Arrua, L. A.; Nieto, J. M. L.; Kremenic, G. *Appl. Catal.* **1988**, *37*, 323−338.

(32) Porto, S. P. S.; Fleury, P. A.; Damen, T. C. *Phys. Rev.* **1967**, *154*, 522−526.

(33) Hanaor, D. A. H.; Sorrell, C. C. *J. Mater. Sci.* **2011**, *46*, 855−874.

(34) Li Bassi, A.; Cattaneo, D.; Russo, V.; Bottani, C. E.; Barborini, E.; Mazza, T.; Piseri, P.; Milani, P.; Ernst, F. O.; Wegner, K.; Pratsinis, S. E. *J. Appl. Phys.* **2005**, *98*, 074305−1−9.

(35) Ohsaka, T.; Izumi, F.; Fujiki, Y. *J. Raman Spectrosc.* **1978**, *7*, 321−324.

(36) Lottici, P. P.; Bersani, D.; Braghini, M.; Montenero, A. *J. Mater. Sci.* **1993**, *28*, 177−183.

(37) Tang, H.; Prasad, K.; Sanjines, R.; Schmid, P. E.; Levy, F. *J. Appl. Phys.* **1994**, *75*, 2042−2047.

(38) Burdett, J. K.; Hughbanks, T.; Miller, G. J.; Richardson, J. W.; Smith, J. V. *J. Am. Chem. Soc.* **1987**, *109*, 3639−3646.

(39) Fang, D.; Luo, Z. P.; Huang, K. L.; Lagoudas, D. C. *Appl. Surf. Sci.* **2011**, *257*, 6451−6461.

(40) Busca, G.; Ramis, G.; Amores, J. M. G.; Escribano, V. S.; Piaggio, P. *J. Chem. Soc., Faraday Trans.* **1994**, *90*, 3181−3190.

(41) del Pino, A. P.; Serra, P.; Morenza, J. L. *Appl. Surf. Sci.* **2002**, *197*, 887−890.

(42) Howard, C. J.; Sabine, T. M.; Dickson, F. *Acta Crystallogr., Sect. B* **1991**, *47*, 462−468.

(43) Shirane, G.; Pickart, S. J.; Newnham, R. *J. Phys. Chem. Solids* **1960**, *13*, 166−168.

(44) Tighineanu, A.; Ruff, T.; Albu, S.; Hahn, R.; Schmuki, P. *Chem. Phys. Lett.* **2010**, *494*, 260−263.

(45) Jasieniak, J.; Califano, M.; Watkins, S. E. *ACS Nano* **2011**, *5*, 5888−5902.

(46) Berglund, C. N.; Spicer, W. E. *Phys. Rev.* **1964**, *136*, 1044−1064.

(47) Gobeli, G. W.; Allen, F. G. *Phys. Rev.* **1962**, *127*, 141−149.

(48) Gratzel, M. *Nature* **2001**, *414*, 338−344.

(49) Uda, M.; Nakagawa, Y.; Yamamoto, T.; Kawasaki, M.; Nakamura, A.; Saito, T.; Hirose, K. *J. Electron Spectrosc. Relat. Phenom.* **1998**, *88*, 767−771.

(50) Bonard, J. M.; Maier, F.; Stockli, T.; Chatelain, A.; de Heer, W. A.; Salvetat, J. P.; Forro, L. *Ultramicroscopy* **1998**, *73*, 7−15.

(51) Lee, C. J.; Lee, T. J.; Lyu, S. C.; Zhang, Y.; Ruh, H.; Lee, H. J. *Appl. Phys. Lett.* **2002**, *81*, 3648−3650.

(52) Munoz, A. G.; Chen, Q.; Schmuki, P. *J. Solid State Electrochem.* **2007**, *11*, 1077−1084.